

## Triphase Interface Synthesis of Plasmonic Gold Bellflowers as Near-Infrared Light Mediated Acoustic and Thermal Theranostics

Peng Huang<sup>†,¶</sup>, Pengfei Rong<sup>†,‡,§,||</sup>, Jing Lin,<sup>†</sup> Wanwan Li,<sup>†</sup> Xuefeng Yan,<sup>†</sup> Molly Gu Zhang,<sup>†</sup> Liming Nie,<sup>†,§</sup>, Gang Niu,<sup>†</sup> Jie Lu,<sup>†</sup> Wei Wang,<sup>†</sup> and Xiaoyuan Chen<sup>\*,†</sup>

<sup>†</sup>Laboratory of Molecular Imaging and Nanomedicine (LOMIN), National Institute of Biomedical Imaging and Bioengineering (NIBIB), National Institutes of Health, Bethesda, Maryland 20892, United States

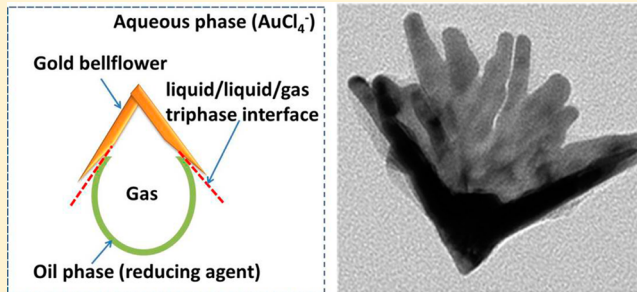
<sup>‡</sup>State Key Laboratory for Powder Metallurgy, Central South University, Changsha, Hunan 410083, China

<sup>§</sup>Center for Molecular Imaging and Translational Medicine, State Key Laboratory of Molecular Vaccinology and Molecular Diagnostics, School of Public Health, Xiamen University, Xiamen 361005, China

<sup>||</sup>Department of Radiology, The Third Xiangya Hospital, Central South University, Changsha, Hunan 410013, China

### Supporting Information

**ABSTRACT:** We present a novel gold bellflower (GBF) platform with multiple-branched petals, prepared by a liquid–liquid–gas triphase interface system, for photoacoustic imaging (PAI)-guided photothermal therapy (PTT). Upon near-infrared (NIR) laser irradiation, the GBFs, with strong NIR absorption, showed very strong PA response and an ultrahigh photothermal conversion efficiency ( $\eta$ , ~74%) among the reported photothermal conversion agents. The excellent performance in PAI and PTT is mainly attributed to the unique features of the GBFs: (i) multiple-branched petals with an enhanced local electromagnetic field, (ii) long narrow gaps between adjacent petals that induce a strong plasmonic coupling effect, and (iii) a bell-shaped nanostructure that can effectively amplify the acoustic signals during the acoustic propagation. Besides the notable PTT and an excellent PAI effect, the NIR-absorbing GBFs may also find applications in NIR light-triggered drug delivery, catalysis, surface enhanced Raman scattering, stealth, antireflection, IR sensors, telecommunications, and the like.



### 1. INTRODUCTION

The fascinating physicochemical properties of nanomaterials promise to syncretize disease treatments and real-time diagnostics into a single theranostic platform for the goal of personalized medicine.<sup>1–8</sup> Intelligent activation with internal or external stimuli such as pH, temperature, redox potential, magnetism, ultrasound, laser light, or enzymatic action have been proposed as “smart” theranostics,<sup>8–13</sup> which could promote a revolution in clinical solutions to achieve prewarning and the early diagnosis of diseases followed by individualized treatment. Particularly, photoactivated theranostics, combining phototherapies (such as photothermal, photodynamic, or phototriggered chemo or gene therapy) with real-time photodiagnosis (such as bioluminescence, fluorescence, optical, or photoacoustic imaging) have been actively pursued because of the advantage of spatiotemporal selectivity and specificity for disease destruction, and the advantages of optical imaging including real-time, nonionizing radiation and high spatial and temporal resolution.<sup>14–20</sup>

Among phototherapies, photothermal therapy (PTT) that employs photothermal conversion agents (PTCAs) to “cook” cancer tissues and cells upon laser irradiation has been increasingly recognized as a promising alternative to the

conventional approaches for cancer treatment.<sup>21–23</sup> An ideal PTCA should exhibit good biocompatibility, strong absorption in the near infrared region (NIR), and high photothermal conversion efficiency to convert the absorbed light into heat.<sup>5</sup> The ability to noninvasively visualize the *in vivo* behavior of the PTCA is especially crucial to design and optimize personalized PTT.<sup>24,25</sup> Unfortunately, most PTCAs are not suitable as contrast agents by themselves, but require fluorescent dye<sup>26,27</sup> or radionuclide labeling.<sup>28,29</sup> Therefore, the development of PTCAs with a natural imaging contrast function and high photothermal conversion efficiency is highly desirable.

Most optical imaging modalities have limited penetration in biological tissues.<sup>30,31</sup> Photoacoustic imaging (PAI), which is based on nonionizing laser pulses and ultrasonic emission detection, can partially offset the limitations incurred by optical imaging.<sup>32,33</sup> In principle, upon pulsed laser irradiation, tissues or contrast agents absorb light and generate a pressure rise by localized thermoelastic expansion, then emit broadband acoustic waves during contraction that can be detected by traditional ultrasound transducers and processed with similar

Received: February 10, 2014

Published: May 19, 2014

reconstruction algorithms.<sup>34,35</sup> Therefore, the combination of PAI and PTT allows for online guidance of the delivery of PTCA and monitoring of the treatment response.

The photothermal conversion mechanism of nanocrystals is related to their internal mobile carriers (electrons or holes), which are strongly driven by the laser electric field, and turns the laser energy into heat.<sup>36</sup> It is worth noting that metal nanocrystals can efficiently convert optical energy into heat based on plasmon resonance enhanced heat conversion.<sup>36</sup> Particularly, gold nanocrystals with various sizes and shapes (such as nanoshells, nanorods, nanocages, nanostars, etc.) have shown great potential to tune their localized surface plasmon resonance (LSPR) to the NIR region.<sup>37–42</sup> For example, the LSPR of gold nanoshells and nanocages can be red-shifted by tuning the core or cavity diameter and shell thickness.<sup>41</sup> Gold nanorods, nanoprisms, and nanoplates have red-shifted LSPR as a result of increased length or edge size.<sup>41</sup> Many uniquely shaped gold nanocrystals have thus been used as contrast agents for optical imaging and as PTCAs for PTT.<sup>43–47</sup> Therefore, the development of novel gold nanostructures with well-designed surface geometry promises to combine imaging contrast function and high photothermal conversion efficiency together.

Inspired by the architectures of bell and bellflower, bell-shaped structures can effectively amplify the acoustic signals during the acoustic propagation in daily life. Here we designed and prepared gold bellflowers (GBFs) with multiple-branched petals through a liquid–liquid–gas triphase interface system produced by ultrasound-inducing vacuum bubbles in a two-phase liquid–liquid system. By taking advantage of the ultrastrong NIR absorbance and ultrahigh photothermal conversion efficiency ( $\eta = 74\%$ , the highest among all of the reported PTCAs), the PAI and photothermal therapy efficacy of GBFs in cancer were presented.

## 2. EXPERIMENTS

**2.1. Preparation of GBFs.** A novel liquid–liquid–gas triphase interface system was employed to prepare the GBFs. In a typical synthesis, HAuCl<sub>4</sub> aqueous solution (0.8 mM) was heated at 50 °C for 5 min, and then 20 mM *o*-phenetidine (TCI America, >98%) in hexane was gently added on top of the HAuCl<sub>4</sub> aqueous solution. The volume ratio of water/hexane is 2:1. Then the two-phase system was sonicated at 50 °C for 30 min (operating frequency of 42 ± 6% kHz and power of 135 W) using the Bransonic Ultrasonic Cleaner 5510R-DTH system. Afterward, the system was transferred to an ice bath, and the same sonication condition was kept for another 60 min. The product was collected by centrifugation at 9000 rpm for 10 min and was washed three times with deionized water. After that, 100 μL of 10 mM HS-PEG-NH<sub>2</sub> (MW = 3400, Nanocs, Inc.) solution was added. The reaction mixture was stirred at room temperature for another 2 h. The mixture was centrifuged and washed three times with deionized water to obtain PEGylated GBFs in aqueous solution.

**2.2. Characterization of GBFs.** The size, morphology, and nanostructure of GBFs were observed by a Hitachi SU-70 Schottky field emission gun scanning electron microscope (FEG-SEM) and a Tecnai TF30 transmission electron microscope (TEM) (FEI, Hillsboro, OR) equipped with a Gatan Ultrascan 1000 CCD camera (Gatan, Pleasanton, CA). Samples for the SEM and TEM were prepared by casting 5–10 μL of GBF aqueous solution on silicon wafers and on 300 mesh copper grids covered with carbon film, respectively, and then by drying at room temperature. UV-vis–NIR spectra were recorded on a Genesys 10S UV-vis spectrophotometer (Thermo Scientific, Waltham, MA) using quartz cuvettes with an optical path of 1 cm. Thermal imaging was taken by a SC300 infrared camera (FLIR, Arlington, VA) and analyzed by Examin IR image software (FLIR).

**2.3. NIR Laser-Induced Heat Conversion.** The aqueous solution of GBFs with different optical densities (ODs) (0.1–1) were irradiated by a 808 nm laser at a power density of 1 W/cm<sup>2</sup> for 5 min. GBFs (OD 808 nm = 0.5) were irradiated by different laser power densities (0.1–2 W/cm<sup>2</sup>). The temperature elevation of the aqueous solutions of gold nanorods (GNRs) and GBFs was recorded as a function of the amount of time they were exposed to laser irradiation (808 nm, 1 W/cm<sup>2</sup>). Pure water was used as a negative control. The laser spot was adjusted to cover the whole surface of the samples. Real-time thermal imaging of the samples was recorded using a FLIR thermal camera and was quantified by FLIR Examiner software.

**2.4. Calculation of the Photothermal Conversion Efficiency ( $\eta$ ).** The photothermal conversion efficiency ( $\eta$ ) of GBFs was calculated according to the reported method.<sup>48–51</sup>

**2.5. Photoacoustic (PA) Properties of GBFs.** PA signal intensity ( $P$ ) can be expressed as the following:<sup>52,53</sup>

$$P = \Gamma F \mu_a$$

Where  $\Gamma$  is the Grüneisen parameter,  $F$  is laser fluence applied, and  $\mu_a$  is the absorption coefficient of imaging target. The Grüneisen parameter increases linearly with temperature and is expressed in the following equation.

$$\Gamma = A + B \times T$$

Where  $A$  and  $B$  are constants at all times, and  $T$  is the temperature at the imaging position. Therefore,  $P$  is linearly related to  $T$ . Generally, the PA signal increases about 4% when the temperature increases one Celsius degree.<sup>54</sup>

**2.6. NIR Laser-Induced PTT Effect in Vitro.** 4T1, HeLa, SCC7, and CHO cells were cultured in standard cell media that were recommended by American type culture collection (ATCC). For PTT in vitro, 4T1 cells were incubated with and without GBFs (100 μg/mL) for 4 h and then were irradiated by an 808 nm laser at different power densities (0.1, 1, and 2 W/cm<sup>2</sup>) for 5 min. The cells were costained with Calcein AM and propidium iodide (PI) for 30 min, washed with phosphate-buffered saline (PBS), and then imaged by an Olympus IX81 motorized inverted microscope.

To further confirm the cytotoxicity and the PTT efficacy of GBFs, an MTT assay was carried out to determine the cell viabilities under various conditions. Cells were seeded into 96 well plates and incubated with different concentrations of GBFs for 24 h at 37 °C in a humidified 5% CO<sub>2</sub> atmosphere. For in vitro PTT, 4T1 cells were incubated with and without GBFs (100 μg/mL) for 4 h at 37 °C under the same conditions and then irradiated by an 808 nm laser (0.1, 1, and 2 W/cm<sup>2</sup>) for 5 min. After illumination, the cells were incubated for another 24 h. The dark control group was under an identical experimental set up except for laser irradiation.

**2.7. Photothermal and Photoacoustic Imaging of GBFs in Vivo.** All animal operations complied with the institutional animal use and care regulations of the National Institutes of Health (NIH). A subcutaneous 4T1 tumor was established by injecting a suspension of  $2 \times 10^6$  4T1 cells in PBS (60 μL) into the flank of each female nude mouse (6 weeks old, 20–25 g) and was allowed to grow for 10–14 days when the tumor size reached ~60 mm<sup>3</sup>. GBFs (400 μg/mL, 50 μL) were intratumorally injected into the tumor-bearing mice and PAI was carried out by a VisualSonic Vevo 2100 LAZR system equipped with a 40 MHz, 256-element linear array transducer. Thermal Imaging was recorded by a SC300 infrared camera (FLIR) when the tumors were exposed to the 808 nm laser (LASERGLOW Technologies) with a power density of 0.5 or 1 W/cm<sup>2</sup> for 10 min.

**2.8. In Vivo PTT Cancer Treatment.** When the tumor size reached ~60 mm<sup>3</sup>, the 4T1 tumor mice were randomly divided into 6 groups (5–7 mice/group). For the treatment groups ( $n = 7$ /group), mice were intratumorally injected with GBFs (400 μg/mL, 50 μL) and then irradiated by the 808 nm laser (0.5 or 1 W/cm<sup>2</sup>) for 5 min. The control groups of mice included untreated mice (control,  $n = 6$ ), mice with PBS administration subjected to laser irradiation only (PBS + 0.5 W/cm<sup>2</sup>,  $n = 6$ ), mice with GBF administration but no laser (GBFs only,  $n = 6$ ), and mice with GNR (50 μL, 400 μg/mL) administration and 808 nm 0.5 W/cm<sup>2</sup> laser irradiation (GNR + 0.5 W/cm<sup>2</sup>,  $n = 5$ ).

The tumor sizes were measured every other day after the treatment. Tumor volume ( $V$ ) was determined by the following equation:  $V = ab^2/2$ , where  $a$  is the length and  $b$  is the width of the tumor. The relative tumor volume was normalized to its initial size before GBF administration and laser irradiation.

### 3. RESULTS AND DISCUSSION

**3.1. Synthesis and Characterization of Plasmonic GBFs.** The GBFs were prepared through a novel liquid–liquid–gas triphase interface system produced by ultrasound-induced vacuum bubbles in a two-phase liquid–liquid system. The representative TEM and SEM images in Figure 1a–d

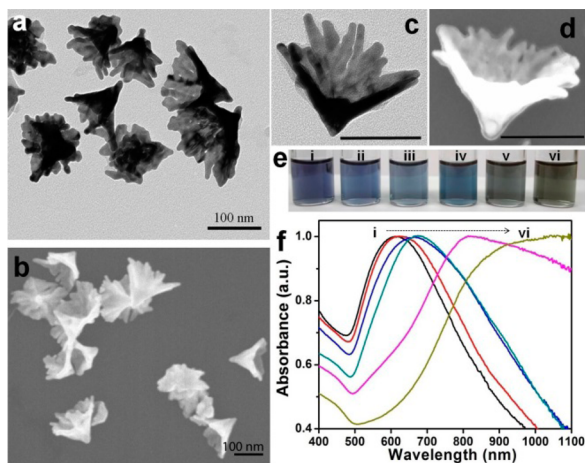


**Figure 1.** Characterization of plasmonic GBFs. TEM (a, c) and SEM (b, d) images of GBFs. (e) Vials containing the GBFs prepared at different time points (i, 0.5; ii, 1; iii, 2; iv, 5; v, 60; vi, 90 min) and (f) the corresponding UV–vis–NIR absorbance spectra. Scale bar, 100 nm.

showed the well-defined bellflower shape with multiple-branched petals (over 10) (Figure S1 of the Supporting Information) and long narrow gaps (1–2 nm) (Figure S2) between adjacent petals, which is similar to the structure of bellflowers (see Figure S3 for more images). The GBFs show hollow cavities with a wide opening from the conical tip to the scraggly bottom side (Figure S7). Interestingly, we also found that the GBFs solution retained its full heat conversion capability even after five cycles of laser heating (Figure S8). The diameter of the circular bottom is  $144.6 \pm 21.8$  nm, the length of the beveled edge is  $123.3 \pm 21.3$  nm, and the thickness is  $10.0 \pm 1.6$  nm. The hydrodynamic diameters of GBFs and PEGylated GBFs measured by the dynamic light scattering (DLS) method were  $179.9 \pm 14.1$  and  $314.3 \pm 27.6$  nm, respectively (Figure S4). The growth process of GBFs is accompanied by a color change of the solution from blue to dark gray (Figure 1e). The corresponding optical properties of the aqueous dispersions were detected using UV–vis–NIR spectroscopy (Figure 1f). The characteristic LSPR peak displays a time-dependent red shift (Figure S5), indicating the growth of GBFs over time, especially the extension of the multiple-branched petals with sharp tips (Figure S6). Encouragingly, when the reaction time is over 60 min, the particles exhibit a strong plasmon band around 800 nm, which makes it highly promising as a PTCA for PTT using an 808 nm laser.

**3.2. Growth Patterns of GBFs.** The original method of the two-phase liquid–liquid system for colloidal synthesis may date back to 1857, in which Faraday first fabricated the dispersed

gold particles by reducing an aqueous gold salt with phosphorus in carbon disulfide.<sup>55,56</sup> Later, the liquid–liquid systems were frequently used to fabricate various nanocrystals.<sup>57–61</sup> Among the reported liquid–liquid systems, organic layers mainly include hexane, toluene, or other nonpolar solvents. In our case, reacted molecular precursors were spatially separated in the hexane or toluene (reducing agent) and the aqueous phases ( $\text{AuCl}_4^-$ ). Upon ultrasound irradiation, because of the cavitation and nebulization between the ultrasound and solvent media, the redox reaction mostly occurred along the liquid–liquid–gas triphase interface with extremely high temperature and pressure. Two different growth patterns were found in our system (Figure 2) including (i)

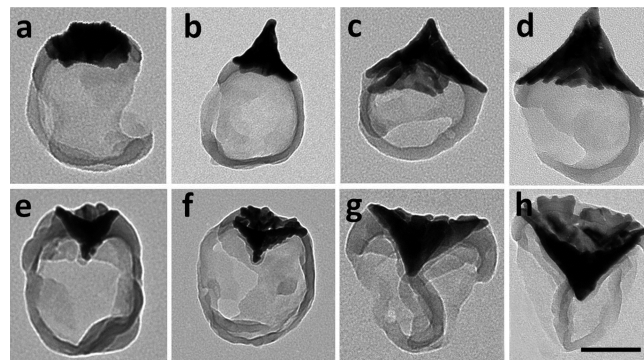


**Figure 2.** TEM images of the growth patterns of GBFs in the liquid–liquid–gas triphase interface system. A redox reaction occurs along the liquid–liquid–gas triphase interface of the outward flange bubbles (a–d); a redox reaction occurs along the liquid–liquid–gas triphase interface of the concave bubbles (e–h). Scale bar, 100 nm.

growth along the liquid–liquid–gas triphase interface of the outward flange bubbles (Scheme S1 of the Supporting Information) and (ii) growth along the liquid–liquid–gas triphase interface of the concave bubbles. This concept of a multiphase interface reaction may be applicable in the study of other chemical reactions existing at multiphase interfaces, and may guide facile preparation of hierarchical micro- or nanostructures.

**3.3. Photothermal Conversion and Photoacoustic Properties of GBFs.** GBFs with strong NIR absorbance around 800 nm motivated us to investigate their dual potential as a PTCA and a PA contrast agent with an 808 nm laser excitation. For PTCA function, aqueous solutions of GBFs at different ODs were exposed to the 808 nm NIR laser at a power density of  $1 \text{ W/cm}^2$  for 5 min, and then the laser was turned off. An obvious concentration-dependent temperature increase was observed (Figure 3a). The rapid cooling of the solutions after the laser was turned off suggests a good thermal conductivity of GBFs. Meanwhile, GBF aqueous solutions at the same  $\text{OD}_{808 \text{ nm}}$  of 0.5 were exposed to the 808 nm NIR laser at different power densities from 0.1 to  $2 \text{ W/cm}^2$  for 5 min. An obvious laser power-dependent temperature increase was observed in Figure 3b. The photothermal effect of GBFs could increase monotonically with particle concentration and radiant energy. In comparison, the well-known GNR PTCA was used as a positive control<sup>62</sup> (Figure 3c). No obvious temperature change was observed for pure water. Upon the 808 nm NIR laser irradiation for 5 min ( $1 \text{ W/cm}^2$ ), GNRs and GBFs raised the temperature by  $24.0$  and  $72.8^\circ\text{C}$ , respectively. Next, we measured the  $\eta$  value of the GBFs according to the

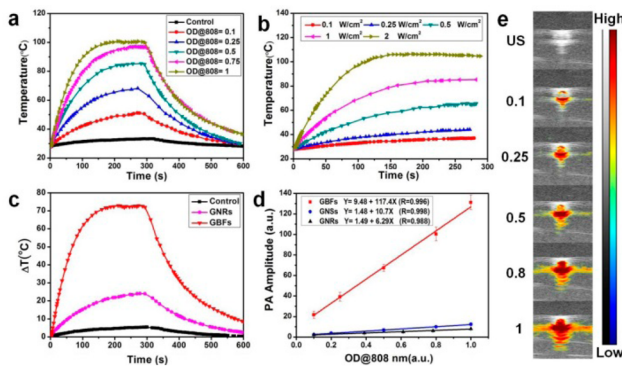


**Figure 3.** Photothermal conversion and photoacoustic properties of GBFs. NIR laser-induced heat generation of aqueous solution of GBFs (a) with the same laser power density of  $1 \text{ W/cm}^2$  and different ODs at 808 nm and (b) with the same OD<sub>808 \text{ nm}</sub> value of 0.5 and irradiated at different laser power densities. (c) Temperature elevation of the aqueous solutions of GNRs and GBFs exposed to an 808 nm laser (OD<sub>808 \text{ nm}</sub> = 1,  $1 \text{ W/cm}^2$ ) as a function of irradiation time. The irradiation lasted for 5 min, and then the laser was turned off. Pure water was used as a negative control. (d) PA signals of GBFs, GNRs, and gold nanostars (GNSs) as a function of OD. (e) PA images of GBFs at different OD<sub>808 \text{ nm}</sub> values.

energy balance on the system by the model reported previously.<sup>48–51</sup> The  $\eta$  value of the GBFs was determined to be 74% (Figure S9 of the Supporting Information), which is the highest among all of the reported PTCAs, such as gold nanoshells (13%), gold vesicles (18%), GNRs (22%), gold hexapods (29.6%), biodegradable gold vesicles (37%), gold nanocages (63%), and so on (Table S1 of the Supporting Information). The ultrahigh  $\eta$  value of the GBFs may be attributed to their structure with multiple-branched petals that act as “lightning rods” to greatly enhance the local electromagnetic field, and long narrow gaps between adjacent petals that induce a strong plasmonic coupling effect. The above results suggest that GBFs can absorb and convert the 808 nm laser energy into heat with ultrahigh efficiency.

The PA signal intensity was linearly correlated with the GBF concentration ( $R^2 = 0.996$ ). Compared to the GNRs (well-known PTCA, LSPR peak at 808 nm) and gold nanostars (GNSs) (with multiple-branched structures, LSPR peak at 808 nm), GBFs showed a much stronger PA signal at the same OD<sub>808 \text{ nm}</sub> value (Figure 3d,e). The linear slope of the GBFs is 117.4, which is markedly higher than that of the GNRs (6.29) and the GNSs (10.7), suggesting that GBFs can be a promising PA contrast agent. The PA signal is linearly correlated with the temperature at the imaging position.<sup>52,53</sup> The PA signal increases by about 4% when the temperature is elevated by one °C.<sup>54</sup> In our case, since the GBFs produce much more heat, which leads to higher temperature, it is no surprise that the PA signal amplification by the GBFs is significantly higher than those of the GNRs and GNSs. The excellent PA property of the GBFs may be attributed to ultrahigh photothermal conversion efficiency (74%) and the GBFs with a bell-shaped nanostructure that can effectively amplify the acoustic signals during the acoustic propagation.

**3.4. In Vitro Photothermal Therapy.** Encouraged by the ultrahigh  $\eta$  value (74%) and the excellent PA response of the GBFs in phantom studies, we next investigated the in vitro PTT efficacy and cytotoxicity of GBFs. Calcein AM (green) and PI (red) containing was used to differentiate the live and

dead cells after PTT (Figure 4a). In the laser only group ( $2 \text{ W/cm}^2$ ) and the GBF only group, no cell killing was found as all of the cells displayed a green fluorescence. In comparison, most of the cells were destroyed after incubation with  $100 \mu\text{g/mL}$  of GBFs and exposure to the NIR laser ( $1 \text{ W/cm}^2$ , 5 min). When the laser power was increased to  $2 \text{ W/cm}^2$ , essentially all of cells were killed, as indicated by the intense homogeneous red fluorescence. In addition, only cells within the laser spot were found to be dead, while cells outside the region of laser spot remained alive.

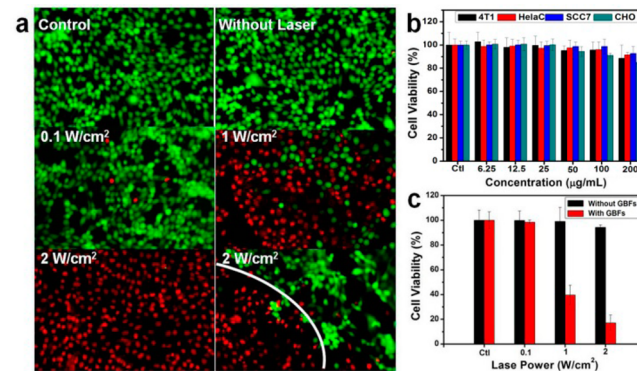


**Figure 4.** In vitro cell experiments. (a) Calcein AM and PI containing of the 4T1 cells without and with incubation with GBFs ( $100 \mu\text{g/mL}$ ) for 4 h before exposure to an 808 nm laser at different power densities. (b) Relative viabilities of the 4T1, HeLa, SCC7, and CHO cells after incubation with GBFs for 24 h. (c) Relative viabilities of the 4T1 cells after GBF-induced photothermal therapy at different laser power densities. Error bars were based on the standard deviations of five parallel samples.

An MTT assay was carried out to further verify the cytotoxicity and PTT efficacy of the GBFs. Upon the exposure of the tumor cells (4T1, Hela, and SCC7) and normal cells (CHO) to the GBFs for 24 h without laser irradiation, the GBFs exhibited negligible toxicity to all four types of cells at all of the studied concentrations (Figure 4b). Upon laser irradiation, the GBFs induced a laser dose-dependent cytotoxicity to the 4T1 cells, in accordance with the results from the Calcein AM and PI costaining.

**3.5. In Vivo Photothermal and Photoacoustic Imaging.** On the basis of the promising in vitro results, we next studied GBFs for in vivo photothermal and PAI in a 4T1 tumor xenograft model. When the tumor volume reached about  $60 \text{ mm}^3$ , the mice were intratumorally injected with GBFs ( $400 \mu\text{g/mL}$ ,  $50 \mu\text{L}$ ). An IR thermal camera was employed to monitor the temperature in vivo (Figure 5a,c). Upon 808 nm laser irradiation at a power of  $0.5 \text{ W/cm}^2$ , the local tumor temperature increased to about  $52^\circ\text{C}$  within 10 min, which is sufficient to kill tumor cells in vivo. Upon  $1 \text{ W/cm}^2$  of 808 nm laser irradiation, the local tumor temperature reached over  $80^\circ\text{C}$  within 10 min. The other parts of the body without laser irradiation experienced a negligible temperature increase. In contrast, the local temperature of the tumor treated with a PBS injection followed by 10 min of laser irradiation was raised by about  $7^\circ\text{C}$ .

PA imaging was employed to monitor the needle-guided intratumoral injection of GBFs. Intense PA signals were observed in the tumor region injected with GBFs (Figure 5b) (see Figure S10 of the Supporting Information for more 3D PA

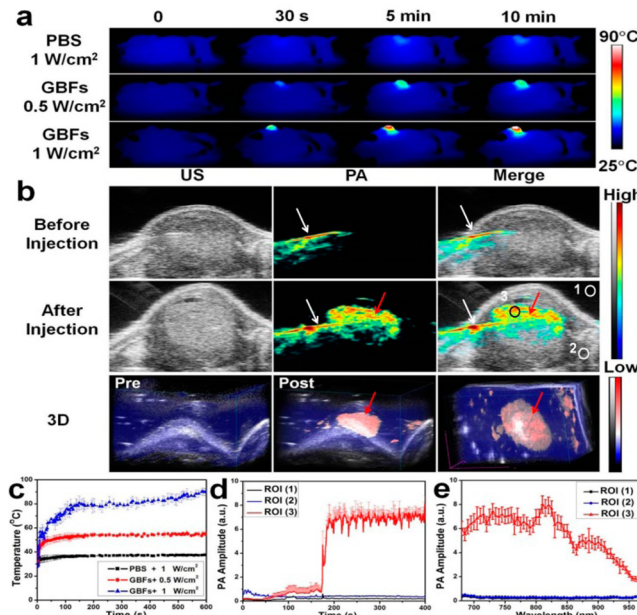


**Figure 5.** In vivo photothermal and PA imaging. (a) Thermal images of 4T1 tumor mice with GBF injection and exposure to an 808 nm laser. As a control, thermal images of mice with PBS injection and exposure to an 808 nm laser at the power density of 1 W/cm<sup>2</sup> were taken. (b) 2D ultrasonic (US) and PA images and 3D PA images of tumor tissues pre- and post-injection of GBFs (white arrow, needle; red arrow, GBFs). (c) Heat curves of 4T1 tumors upon laser irradiation as a function of irradiation time. (d) Time-lapse PA signal change followed by intratumoral injection of GBFs. (e) PA spectra of GBFs after injection.

images). As shown in Figure 5d, the average tumor PA intensity ( $6.95 \pm 0.33$  au) of GBFs was ~17-fold stronger than that before GBF injection ( $0.40 \pm 0.03$  au). The PA spectrum of GBFs after they were injected into the tumor shows a peak similar to one in its UV-vis-NIR spectrum (Figure 5e and Figure 1g), which indicates that the optical property of GBFs after they were injected *in vivo* was without any change.

**3.6. In Vivo Photothermal Therapy.** Finally, the GBF-induced PTT effect *in vivo* was studied. It is well-known that large particles are cleared rapidly by macrophages of the reticuloendothelial system (RES).<sup>63–65</sup> Therefore, the preferred route of GBF administration is a local injection, especially an intratumoral injection for tumor ablation, which is the most efficient mode of delivery of a PTCA in PTT.<sup>66–68</sup>

As shown in Figure 6a, six groups of 4T1 tumor mice with 5–7 mice per group were used in our experiment. For the treatment groups ( $n = 7/\text{group}$ ), mice were intratumorally injected with GBFs (400  $\mu\text{g}/\text{mL}$ , 50  $\mu\text{L}$ ) and then irradiated by the 808 nm laser at power densities of 0.5 or 1 W/cm<sup>2</sup> for 5 min. Other control groups of mice included untreated mice (control,  $n = 6$ ), mice with PBS administration subjected to laser irradiation only (PBS + 0.5 W/cm<sup>2</sup>,  $n = 6$ ), mice with GBF administration but no laser (GBFs only,  $n = 6$ ), and mice with GNR administration and subjected to 808 nm 0.5 W/cm<sup>2</sup> laser irradiation (GNR + 0.5 W/cm<sup>2</sup>,  $n = 5$ ). Both the GNR and GBF administration and irradiation groups showed a significant delay in tumor growth or complete tumor regression compared to the control groups after 2 weeks (GNR vs control,  $P < 0.001$ ; GBF vs control,  $P < 0.0001$ ). In the GBFs and laser groups (both 0.5 and 1 W/cm<sup>2</sup>), all of the tumors were effectively ablated, leaving black scars at their original sites without

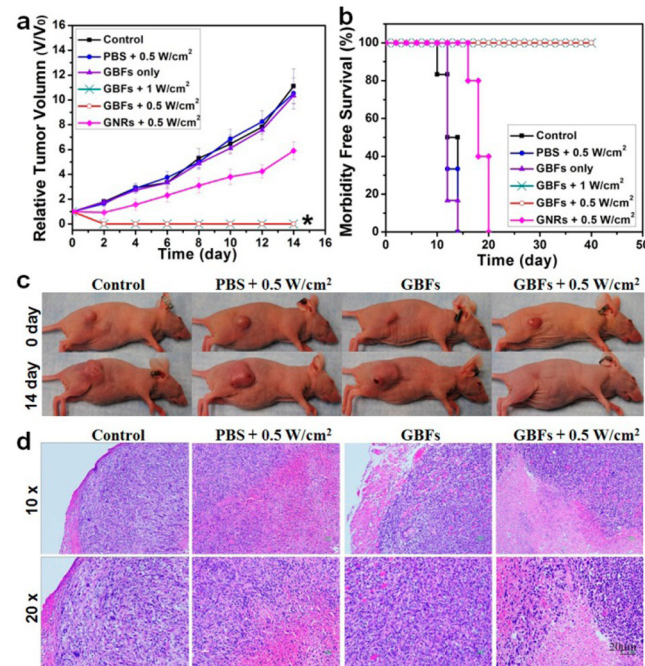


**Figure 6.** In vivo PTT. (a) Relative 4T1 tumor volume after various treatments. Tumor volumes were normalized to their initial sizes. Error bar, standard deviation of 5–7 mice. \* $P < 0.01$ . (b) Survival curves of the 4T1 tumor mice after various treatments. GBF-treated mice after PTT treatment showed complete tumor regression and 100% survival over 40 days. (c) Photographs of the 4T1 tumor mice on different days after the GBF treatment. (d) Hematoxylin and eosin (HE) staining of tumor sections collected from different treatment groups of mice at day 1.

showing reoccurrence (Figure 6c and Figure S11 of the Supporting Information).

It is worth noting that with low dose of laser irradiation (0.5 W/cm<sup>2</sup> for 5 min), the GBF group exhibited significantly higher therapeutic efficacy than did the GNR group on day 14 (GBF vs GNR,  $P < 0.0001$ ). While mice in the control groups showed average life spans of ~14 days once the treatment started, mice in the GBF-treated groups were tumor-free and survived over 40 days, mice in the GNR and laser group showed only slight delay of tumor growth and all of the animals had to be sacrificed on day 20 because of the tumor burden (Figure 6b). Moreover, no significant body weight variation was noticed after the GBF PTT treatment (Figure S12 of the Supporting Information). In addition, tumors were also collected for HE staining one day after treatment (Figure 6d). In the PBS control and GBFs only control groups, no change was observed. In the PBS and laser group, there was an observable erythema and a small number of inflammatory cell infiltrations without tissue structure damage. In contrast, we found a large number of inflammatory cell infiltrations, cell death, and erythema with serious tissue structure damage in the GBF and laser group. In the high resolution HE images (Figure S13 of the Supporting Information), we found significant cancer cell damage with a breakup of the nuclear membrane and shrinkage of the nuclei with karyorrhexis and pyknosis. These results indicate that GBFs have excellent theranostic capability for both PT and PA imaging and PTT of tumor. Since some of the intratumorally-injected nanoparticles would leak into circulation and accumulate in the RES,<sup>69–71</sup> we also collected the major organs including the hearts, livers, spleens, lungs, and

kidneys from the mice at 1 day and 2 days post-treatment (Figure S14 of the Supporting Information). No obvious damage or inflammation was observed as compared to the control groups. These results indicate that GBFs are capable of imaging guided photothermal therapy *in vivo*.

## 4. CONCLUSIONS

We have developed a novel theranostic platform based on plasmonic GBFs, prepared by a novel liquid–liquid–gas triphase interface system, for simultaneous effective PA imaging and PTT. The bell-shaped gold nanostructures with multiple-branched petals and long narrow gaps between adjacent petals show excellent PA response and ultrahigh photothermal conversion efficiency. The GBFs we developed have the following features: (i) good biocompatibility, (ii) ultrahigh photothermal conversion efficiency ( $\eta = 74\%$ ), (iii) simultaneous thermal and PA imaging and PTT efficacy. This study is important not only because it provides a novel concept of a multiphase interface reaction that can potentially be applied to investigate other chemical reactions existing at multiphase interfaces and guide facile preparation of hierarchical micro- and nano-structures, but also because it paves the way toward the goal of personalized medicine by the natural structure-inspired construction of functional nanostructures as theranostics.

## ■ ASSOCIATED CONTENT

### Supporting Information

Additional figures and a scheme and table as described in the text. This material is available free of charge via the Internet at <http://pubs.acs.org>.

## ■ AUTHOR INFORMATION

### Corresponding Author

[shawn.chen@nih.gov](mailto:shawn.chen@nih.gov)

### Author Contributions

¶P.H. and P.R. contributed equally to this work.

### Notes

The authors declare no competing financial interest.

## ■ ACKNOWLEDGMENTS

This work was supported, in part, by the Intramural Research Program (IRP) of the NIBIB, NIH, the National Key Basic Research Program (973 Project) (2010CB933901, 2013CB733802, 2014CB744503), and the National Science Foundation of China (81272987, 31170961, 51102258, 81371596).

## ■ REFERENCES

- (1) Xie, J.; Lee, S.; Chen, X. *Adv. Drug Delivery Rev.* **2010**, *62*, 1064.
- (2) Lovell, J. F.; Jin, C. S.; Huynh, E.; Jin, H.; Kim, C.; Rubinstein, J. L.; Chan, W. C. W.; Cao, W.; Wang, L. V.; Zheng, G. *Nat. Mater.* **2011**, *10*, 324.
- (3) Huynh, E.; Zheng, G. *Wiley Interdiscip. Rev.: Nanomed. Nanobiotechnol.* **2013**, *5*, 250.
- (4) Zhang, Z.; Wang, L.; Wang, J.; Jiang, X.; Li, X.; Hu, Z.; Ji, Y.; Wu, X.; Chen, C. *Adv. Mater.* **2012**, *24*, 1418.
- (5) Huang, P.; Lin, J.; Li, W.; Rong, P.; Wang, Z.; Wang, S.; Wang, X.; Sun, X.; Aronova, M.; Niu, G.; Leapman, R. D.; Nie, Z.; Chen, X. *Angew. Chem., Int. Ed.* **2013**, *52*, 13958.
- (6) Koo, H.; Sun, I. C.; Ryu, J. H.; Kim, K.; Kwon, I. C. *Chem. Soc. Rev.* **2012**, *41*, 2656.
- (7) Sun, Z.; Huang, P.; Tong, G.; Lin, J.; Jin, A.; Rong, P.; Zhu, L.; Nie, L.; Niu, G.; Cao, F.; Chen, X. *Nanoscale* **2013**, *5*, 6857.
- (8) Huang, P.; Lin, J.; Wang, X.; Wang, Z.; Zhang, C.; He, M.; Wang, K.; Chen, F.; Li, Z.; Shen, G.; Cui, D.; Chen, X. *Adv. Mater.* **2012**, *24*, 5104.
- (9) Lovell, J. F.; Jin, C. S.; Huynh, E.; MacDonald, T. D.; Cao, W.; Zheng, G. *Angew. Chem., Int. Ed.* **2012**, *124*, 2479.
- (10) Ng, K. K.; Lovell, J. F.; Zheng, G. *Acc. Chem. Res.* **2011**, *44*, 1105.
- (11) Rai, P.; Mallidi, S.; Zheng, X.; Rahmazadeh, R.; Mir, Y.; Elrington, S.; Khurshid, A.; Hasan, T. *Adv. Drug Delivery Rev.* **2010**, *62*, 1094.
- (12) Du, J.; O'Reilly, R. *Chem. Soc. Rev.* **2011**, *40*, 2402.
- (13) Fleige, E.; Quadir, M.; Haag, R. *Adv. Drug Delivery Rev.* **2012**, *64*, 866.
- (14) Gao, X.; Cui, Y.; Levenson, R. M.; Chung, L. W. K.; Nie, S. *Nat. Biotechnol.* **2004**, *22*, 969.
- (15) Janib, S. M.; Moses, A. S.; MacKay, J. A. *Adv. Drug Delivery Rev.* **2010**, *62*, 1052.
- (16) Bechet, D.; Couleaud, P.; Frochot, C.; Viriot, M. L.; Guillemin, F.; Barberi-Heyob, M. *Trends Biotechnol.* **2008**, *26*, 612.
- (17) Lovell, J.; Liu, T.; Chen, J.; Zheng, G. *Chem. Rev.* **2010**, *110*, 2839.
- (18) Yavuz, M. S.; Cheng, Y.; Chen, J.; Cobley, C. M.; Zhang, Q.; Rycenga, M.; Xie, J.; Kim, C.; Song, K. H.; Schwartz, A. G.; Wang, L. V.; Xia, Y. *Nat. Mater.* **2009**, *8*, 935.
- (19) Celli, J. P.; Spring, B. Q.; Rizvi, I.; Evans, C. L.; Samkoe, K. S.; Verma, S.; Pogue, B. W.; Hasan, T. *Chem. Rev.* **2010**, *110*, 2795.
- (20) Park, K.; Lee, S.; Kang, E.; Kim, K.; Choi, K.; Kwon, I. C. *Adv. Funct. Mater.* **2009**, *19*, 1553.
- (21) Zha, Z.; Yue, X.; Ren, Q.; Dai, Z. *Adv. Mater.* **2012**, *25*, 777.
- (22) Yang, K.; Hu, L.; Ma, X.; Ye, S.; Cheng, L.; Shi, X.; Li, C.; Li, Y.; Liu, Z. *Adv. Mater.* **2012**, *24*, 1868.
- (23) Yang, K.; Xu, H.; Cheng, L.; Sun, C.; Wang, J.; Liu, Z. *Adv. Mater.* **2012**, *24*, 5586.
- (24) Zha, Z.; Wang, J.; Qu, E.; Zhang, S.; Jin, Y.; Wang, S.; Dai, Z. *Sci. Rep.* **2013**, *3*, 2360.
- (25) Zha, Z.; Deng, Z.; Li, Y.; Li, C.; Wang, J.; Wang, S.; Qu, E.; Dai, Z. *Nanoscale* **2013**, *5*, 4462.
- (26) Robinson, J. T.; Tabakman, S. M.; Liang, Y.; Wang, H.; Sanchez Casalongue, H.; Vinh, D.; Dai, H. *J. Am. Chem. Soc.* **2011**, *133*, 6825.
- (27) Yang, K.; Zhang, S.; Zhang, G.; Sun, X.; Lee, S.-T.; Liu, Z. *Nano Lett.* **2010**, *10*, 3318.
- (28) Wang, Y.; Black, K. C.; Luehmann, H.; Li, W.; Zhang, Y.; Cai, X.; Wan, D.; Liu, S.-Y.; Li, M.; Kim, P.; Li, Z. Y.; Wang, L. V.; Liu, Y.; Xia, Y. *ACS Nano* **2013**, *7*, 2068.
- (29) Liu, Z.; Cai, W.; He, L.; Nakayama, N.; Chen, K.; Sun, X.; Chen, X.; Dai, H. *Nat. Nanotechnol.* **2006**, *2*, 47.
- (30) Kim, C.; Favazza, C.; Wang, L. V. *Chem. Rev.* **2010**, *110*, 2756.
- (31) Nie, L.; Wang, S.; Wang, X.; Rong, P.; Ma, Y.; Liu, G.; Huang, P.; Lu, G.; Chen, X. *Small* **2014**, *10*, 1585.
- (32) Zhang, H. F.; Maslov, K.; Stoica, G.; Wang, L. V. *Nat. Biotechnol.* **2006**, *24*, 848.
- (33) Huynh, E.; Lovell, J. F.; Helfield, B. L.; Jeon, M.; Kim, C.; Goertz, D. E.; Wilson, B. C.; Zheng, G. *J. Am. Chem. Soc.* **2012**, *134*, 16464.
- (34) Wilson, K. E.; Wang, T. Y.; Willmann, J. K. *J. Nucl. Med.* **2013**, *54*, 1851.
- (35) Wang, L. V.; Hu, S. *Science* **2012**, *335*, 1458.
- (36) Govorov, A. O.; Richardson, H. H. *Nano Today* **2007**, *2*, 30.
- (37) Huang, X.; Jain, P. K.; El-Sayed, I. H.; El-Sayed, M. A. *Lasers Med. Sci.* **2008**, *23*, 217.
- (38) Lal, S.; Clare, S. E.; Halas, N. *J. Acc. Chem. Res.* **2008**, *41*, 1842.
- (39) Zeng, J.; Goldfeld, D.; Xia, Y. *Angew. Chem., Int. Ed.* **2013**, *52*, 4169.
- (40) Chen, J.; Glaus, C.; Laforest, R.; Zhang, Q.; Yang, M.; Gidding, M.; Welch, M. J.; Xia, Y. *Small* **2010**, *6*, 811.
- (41) Ye, E.; Win, K. Y.; Tan, H. R.; Lin, M.; Teng, C. P.; Mlayah, A.; Han, M.-Y. *J. Am. Chem. Soc.* **2011**, *133*, 8506.

- (42) Huang, P.; Bao, L.; Zhang, C.; Lin, J.; Luo, T.; Yang, D.; He, M.; Li, Z.; Gao, G.; Gao, B. *Biomaterials* **2011**, *32*, 9796.
- (43) Cobley, C. M.; Chen, J.; Cho, E. C.; Wang, L. V.; Xia, Y. *Chem. Soc. Rev.* **2011**, *40*, 44.
- (44) Yuan, H.; Khoury, C. G.; Hwang, H.; Wilson, C. M.; Grant, G. A.; Vo-Dinh, T. *Nanotechnology* **2012**, *23*, 075102.
- (45) Lapotko, D. O.; Lukianova, E.; Oraevsky, A. A. *Lasers Surg. Med.* **2006**, *38*, 631.
- (46) Lukianova-Hleb, E. Y.; Oginsky, A. O.; Samaniego, A. P.; Shenefelt, D. L.; Wagner, D. S.; Hafner, J. H.; Farach-Carson, M. C.; Lapotko, D. O. *Theranostics* **2011**, *1*, 3.
- (47) Lukianova-Hleb, E. Y.; Ren, X.; Townley, D.; Wu, X.; Kupferman, M. E.; Lapotko, D. O. *Theranostics* **2012**, *2*, 976.
- (48) Tian, Q.; Jiang, F.; Zou, R.; Liu, Q.; Chen, Z.; Zhu, M.; Yang, S.; Wang, J.; Wang, J.; Hu, J. *ACS Nano* **2011**, *5*, 9761.
- (49) Tian, Q.; Hu, J.; Zhu, Y.; Zou, R.; Chen, Z.; Yang, S.; Li, R.-W.; Su, Q.; Han, Y.; Liu, X. *J. Am. Chem. Soc.* **2013**, *135*, 8571.
- (50) Liu, Y.; Ai, K.; Liu, J.; Deng, M.; He, Y.; Lu, L. *Adv. Mater.* **2012**, *25*, 1353.
- (51) Hessel, C. M.; Pattani, V. P.; Rasch, M.; Panthani, M. G.; Koo, B.; Tunnell, J. W.; Korgel, B. A. *Nano Lett.* **2011**, *11*, 2560.
- (52) Pramanik, M.; Wang, L. V. *J. Biomed. Opt.* **2009**, *14*, 054024.
- (53) Shah, J.; Park, S.; Aglyamov, S.; Larson, T.; Ma, L.; Sokolov, K.; Johnston, K.; Milner, T.; Emelianov, S. Y. *J. Biomed. Opt.* **2008**, *13*, 034024.
- (54) Ntziachristos, V. *J. Biophotonics* **2013**, *6*, 473.
- (55) Faraday, M. *Philos. Trans. R. Soc.* **1857**, *147*, 145.
- (56) Brust, M.; Walker, M.; Bethell, D.; Schiffrin, D. J.; Whyman, R. J. *Chem. Soc., Chem. Commun.* **1994**, 801.
- (57) Huang, P.; Lin, J.; Li, Z.; Hu, H.; Wang, K.; Gao, G.; He, R.; Cui, D. *Chem. Commun.* **2010**, *46*, 4800.
- (58) He, M.; Huang, P.; Zhang, C.; Chen, F.; Wang, C.; Ma, J.; He, R.; Cui, D. *Chem. Commun.* **2011**, *47*, 9510.
- (59) He, M.; Huang, P.; Zhang, C.; Hu, H.; Bao, C.; Gao, G.; He, R.; Cui, D. *Adv. Funct. Mater.* **2011**, *21*, 4470.
- (60) Zhang, P.; He, J.; Ma, X.; Gong, J.; Nie, Z. *Chem. Commun.* **2013**, *49*, 987.
- (61) He, M.; Huang, P.; Zhang, C.; Ma, J.; He, R.; Cui, D. *Chem.—Eur. J.* **2012**, *18*, 5954.
- (62) Li, Z.; Huang, P.; Zhang, X.; Lin, J.; Yang, S.; Liu, B.; Gao, F.; Xi, P.; Ren, Q.; Cui, D. *Mol. Pharmaceutics* **2009**, *7*, 94.
- (63) Albanese, A.; Tang, P. S.; Chan, W. C. W. *Annu. Rev. Biomed. Eng.* **2012**, *14*, 1.
- (64) De Jong, W. H.; Hagens, W. I.; Krystek, P.; Burger, M. C.; Sips, A. J.; Geertsma, R. E. *Biomaterials* **2008**, *29*, 1912.
- (65) Moghimi, S. M.; Hunter, A. C.; Murray, J. C. *FASEB J.* **2005**, *19*, 311.
- (66) Huang, X.; Peng, X.; Wang, Y.; Wang, Y.; Shin, D. M.; El-Sayed, M. A.; Nie, S. *ACS Nano* **2010**, *4*, 5887.
- (67) Wang, S.; Huang, P.; Nie, L.; Xing, R.; Liu, D.; Wang, Z.; Lin, J.; Chen, S.; Niu, G.; Lu, G.; Chen, X. *Adv. Mater.* **2013**, *25*, 3055.
- (68) He, J.; Huang, X.; Li, Y.-C.; Liu, Y.; Babu, T.; Aronova, M. A.; Wang, S.; Lu, Z.; Chen, X.; Nie, Z. *J. Am. Chem. Soc.* **2013**, *135*, 7974.
- (69) Moon, H. K.; Lee, S. H.; Choi, H. C. *ACS Nano* **2009**, *3*, 3707.
- (70) Lammers, T.; Peschke, P.; Kühnlein, R.; Subr, V.; Ulbrich, K.; Huber, P.; Hennink, W.; Storm, G. *Neoplasia* **2006**, *8*, 788.
- (71) Lin, J.; Wang, S.; Huang, P.; Wang, Z.; Chen, S.; Niu, G.; Li, W.; He, J.; Cui, D.; Lu, G.; Chen, X.; Nie, Z. *ACS Nano* **2013**, *7*, 5320.